nature medicine

DNA methyltransferase 3a regulates osteoclast differentiation by coupling to an S-adenosylmethionine–producing metabolic pathway

Keizo Nishikawa[1–3], Yoriko Iwamoto[1–4], Yasuhiro Kobayashi[5], Fumiki Katsuoka[6,7], Shin-ichi Kawaguchi[8], Tadayuki Tsujita[7], Takashi Nakamura[9], Shigeaki Kato[10], Masayuki Yamamoto[6,7], Hiroshi Takayanagi[11,12] & Masaru Ishii[1–3]

Metabolic reprogramming occurs in response to the cellular environment to mediate differentiation[1–3], but the fundamental mechanisms linking metabolic processes to differentiation programs remain to be elucidated. During osteoclast differentiation, a shift toward more oxidative metabolic processes occurs[3]. In this study we identified the *de novo* DNA methyltransferase 3a (Dnmt3a) as a transcription factor that couples these metabolic changes to osteoclast differentiation. We also found that receptor activator of nuclear factor-κB ligand (RANKL), an essential cytokine for osteoclastogenesis[4–7], induces this metabolic shift towards oxidative metabolism, which is accompanied by an increase in S-adenosylmethionine (SAM) production. We found that SAM-mediated DNA methylation by Dnmt3a regulates osteoclastogenesis via epigenetic repression of anti-osteoclastogenic genes. The importance of Dnmt3a in bone homeostasis was underscored by the observations that *Dnmt3a*-deficient osteoclast precursor cells do not differentiate efficiently into osteoclasts and that mice with an osteoclast-specific deficiency in *Dnmt3a* have elevated bone mass due to a smaller number of osteoclasts. Furthermore, inhibition of DNA methylation by theaflavin-3,3′-digallate abrogated bone loss in models of osteoporosis. Thus, this study reveals the role of epigenetic processes in the regulation of cellular metabolism and differentiation, which may provide the molecular basis for a new therapeutic strategy for a variety of bone disorders.

Although epigenetic regulation is known to be a fundamental mechanism for mediating various cellular processes, epigenetic mechanisms in osteoclastogenesis remain to be elucidated[8,9]. To explore the epigenetic factors involved in osteoclast differentiation, we performed genome-wide screening for mRNAs expressed in bone marrow–derived monocyte-macrophage precursor cells (BMMs, which are also the precursors for osteoclasts) stimulated by RANKL in the presence of macrophage colony-stimulating factor (M-CSF)[10]. Notably, osteoclasts, but not osteoblasts, continuously expressed mRNA for the Dnmt protein *Dnmt3a* (**Fig. 1a** and **Supplementary Fig. 1**). To investigate the role of Dnmts in osteoclastogenesis, we examined the effects of several Dnmt inhibitors on osteoclast differentiation. As mature osteoclasts are formed by the fusion of many mononucleated immature osteoclasts in response to cytokine signaling, we evaluated *in vitro* osteoclast differentiation by counting multinucleated cells (MNCs) positive for the osteoclast marker tartrate-resistant acid phosphatase (TRAP) after stimulation of BMMs with RANKL in the presence of M-CSF[11,12]. Although 5-azacytidine (AzaC) and 5-azadeoxycytidine (AzadC) are widely used as Dnmt inhibitors, azanucleosides cause cytotoxicity because of their incorporation into RNA or genomic DNA. Indeed, treatment with these azanucleosides impaired proliferation of BMMs as well as the formation of TRAP-positive MNCs (**Supplementary Fig. 2a**,**b**). We also used other inhibitors—TF-3 (theaflavin-3,3′-digallate), EGCG (epigallocatechin gallate), and RG108—that prevent Dnmt activity, even though their specificity and efficacy have so far been limited[13,14]. Biochemical analysis showed that both TF-3 and EGCG have stronger inhibitory effects on Dnmt3a and Dnmt3b than on other methyltransferases (**Supplementary Fig. 2c**,**d**). In addition, *in silico* analysis predicted that TF-3 would bind most specifically to the catalytic domain of Dnmt3a (**Supplementary Fig. 2e**,**f**). Treatment with TF-3 or EGCG impaired the formation of TRAP-positive MNCs, whereas RG108 had a negligible effect, probably reflecting a lesser degree of inhibitory activity (**Fig. 1b** and **Supplementary Fig. 2g**). Nevertheless, neither the number of CD11b$^+$ osteoclast precursor cells nor the proliferative

[1]Department of Immunology and Cell Biology, Graduate School of Medicine and Frontier Biosciences, Osaka University, Osaka, Japan. [2]WPI-Immunology Frontier Research Center, Osaka University, Osaka, Japan. [3]Japan Science and Technology Agency, CREST, Tokyo, Japan. [4]Department of Otorhinolaryngology–Head and Neck Surgery, Graduate School of Medicine, Osaka University, Osaka, Japan. [5]Institute for Oral Science, Matsumoto Dental University, Nagano, Japan. [6]Department of Integrative Genomics, Tohoku Medical Megabank Organization, Tohoku University, Sendai, Japan. [7]Department of Medical Biochemistry, Tohoku University Graduate School of Medicine, Sendai, Japan. [8]Department of Molecular Medicine and Therapy, Tohoku University Graduate School of Medicine, Sendai, Japan. [9]Department of Biochemistry, School of Medicine, Keio University, Tokyo, Japan. [10]Soma Central Hospital, Fukushima, Japan. [11]Department of Immunology, Graduate School of Medicine and Faculty of Medicine, University of Tokyo, Tokyo, Japan. [12]Japan Science and Technology Agency, ERATO, Takayanagi Osteonetwork Project, Tokyo, Japan. Correspondence should be addressed to K.N. (nishi@ifrec.osaka-u.ac.jp) or M.I. (mishii@icb.med.osaka-u.ac.jp).

Received 5 July 2014; accepted 20 November 2014; published online 23 February 2015; doi:10.1038/nm.3774

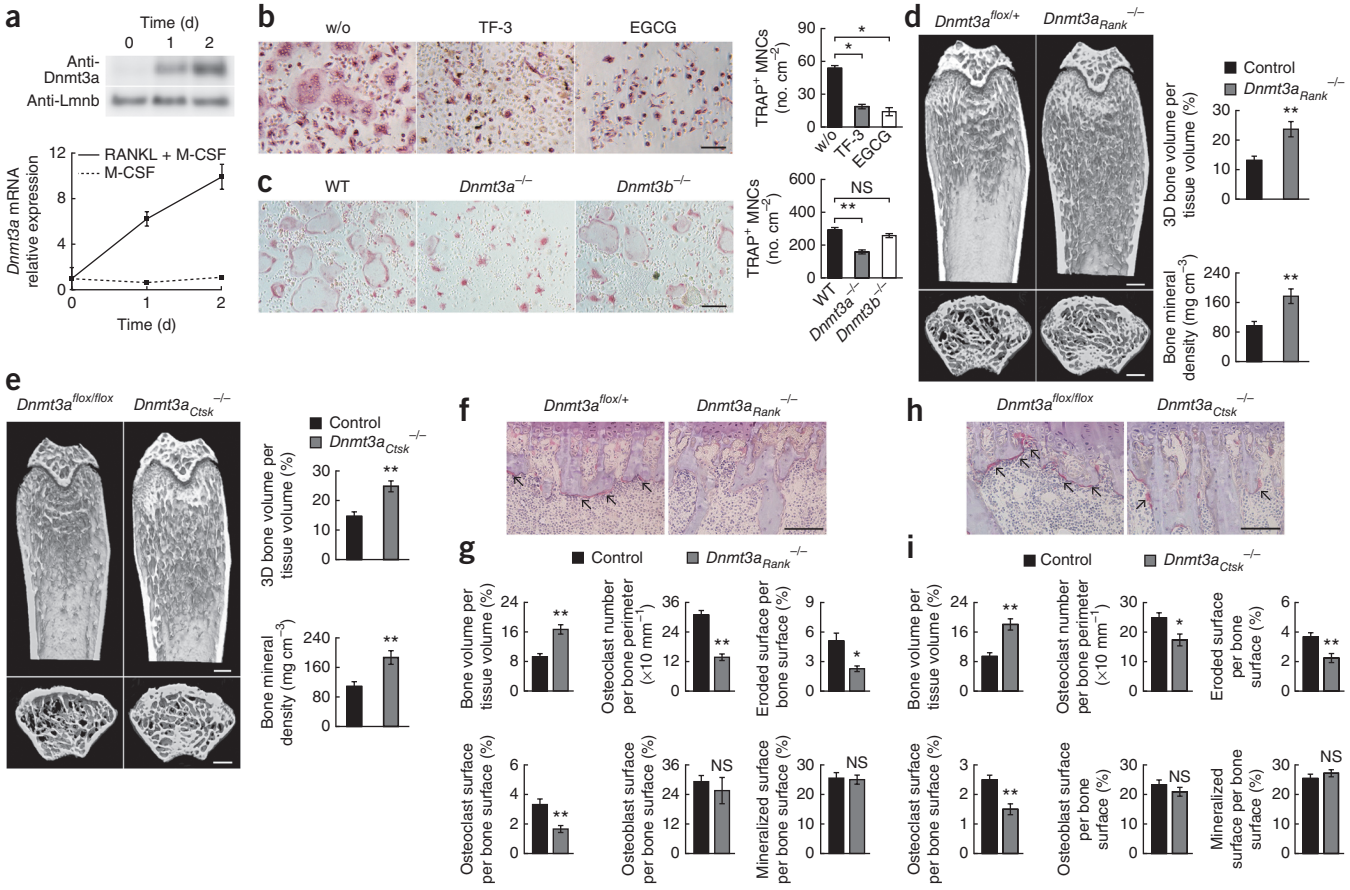

Figure 1 Osteoclast-specific *Dnmt3a*-deficient mice exhibit a high bone mass phenotype. (**a**) Expression of Dnmt3a during osteoclastogenesis, as determined by anti-Dnmt3a immunoblot. Anti-Lmnb was used as the control. Below, a graph showing the relative expression (compared to day 0) of *Dnmt3a* mRNA in unstimulated or RANKL-stimulated BMMs, measured by RT-qPCR analysis. $n = 3$; results representative of more than three experiments. (**b**,**c**) TRAP-stained cells showing (**b**) the effect of Dnmt inhibitors TF-3 (10 μM) and EGCG (25 μM) on osteoclastogenesis and (**c**) the effect of *Dnmt3a* and *Dnmt3b* deficiency on ESC-derived osteoclast formation. Scale bars, 100 μm; images representative of more than three experiments. On right, bar graph shows the number of TRAP+ cells for each condition, obtained from experiments repeated more than three times. w/o, without inhibitors. (**d**,**e**) Microcomputed tomography (μCT) analysis of the femurs of 10-week-old control ($n = 6$; control for $Dnmt3a_{Rank}^{-/-}$), $Dnmt3a_{Rank}^{-/-}$ ($n = 6$), control ($n = 4$; control for $Dnmt3a_{Ctsk}^{-/-}$), $Dnmt3a_{Ctsk}^{-/-}$ ($n = 5$) male mice (top, longitudinal view; bottom, axial view of the metaphyseal region using parameters based on μCT analysis of the metaphyseal region). Scale bars, 0.5 mm. In the graphs, bone volume (upper) and bone mineral density (lower) are compared in the specified mice, as determined by μCT analysis. (**f**,**h**) Histological analysis of the proximal tibias of 10-week-old $Dnmt3a^{flox/+}$, $Dnmt3a^{flox/flox}$, $Dnmt3a_{Ctsk}^{-/-}$ and $Dnmt3a_{Rank}^{-/-}$ male mice. *N* values for each group same as in **g**,**i**. TRAP staining; red with arrows, osteoclasts. Scale bars, 100 μm. (**g**,**i**) Parameters for osteoclastic bone resorption during bone morphometric analysis of 10-week-old control ($n = 5$), $Dnmt3a_{Rank}^{-/-}$ ($n = 5$), control ($n = 8$), and $Dnmt3a_{Ctsk}^{-/-}$ ($n = 8$) male mice. Data denote the mean ± sem. $^*P < 0.05$; $^{**}P < 0.01$; NS, not significant (*t*-test).

or apoptotic activities of BMMs were affected by TF-3 or EGCG (**Supplementary Fig. 2h**), suggesting that *de novo* DNA methylation is important for osteoclast differentiation.

Next, to determine which Dnmt is required for osteoclast differentiation, we performed shRNA-mediated knockdown analysis and found that the introduction of Dnmt3a shRNA, but not Dnmt1 or Dnmt3b shRNA, resulted in a significant blockade of TRAP-positive MNC formation (**Supplementary Fig. 3**). Consistent with this, procainamide, a selective inhibitor of Dnmt1, did not affect TRAP-positive MNC formation (**Supplementary Fig. 2g**). To further investigate the role of Dnmt3a and Dnmt3b in osteoclastogenesis, we evaluated osteoclast differentiation in *Dnmt3a*- and *Dnmt3b*-deficient embryonic stem cells (ESCs). Wild-type (WT), *Dnmt3a*-deficient, and *Dnmt3b*-deficient ESCs differentiated equally into osteoclast precursor cells expressing CD11b (data not shown). However, $Dnmt3a^{-/-}$ ESCs failed to differentiate into osteoclasts, whereas RANKL-induced, TRAP-positive MNCs were observed among *Dnmt3b*-deficient ESCs at a level similar to that of wild-type ESCs (**Fig. 1c**). Thus, Dnmt3a is activated by RANKL and plays an important role in osteoclast differentiation.

These results prompted us to investigate the bone phenotype of mice deficient in *Dnmt3a*. *Dnmt3a*-deficient mice die prematurely and display a runt phenotype[15,16], characteristics likely caused by osteoclast and osteoblast abnormalities. To investigate the role of Dnmt3a in osteoclasts and osteoblasts *in vivo*, we crossed mice with *Dnmt3a* flanked by *loxP* sites ($Dnmt3a^{flox/flox}$ mice[17]) with either $Ctsk^{Cre/+}$ (ref. 18), $Rank^{Cre/+}$ (ref. 19) or *Col1a1–Cre* (ref. 20) mice to specifically disrupt the *Dnmt3a* gene in the osteoclast ($Dnmt3a_{Ctsk}^{-/-}$ and $Dnmt3a_{Rank}^{-/-}$) and osteoblast lineages ($Dnmt3a_{Col1a1}^{-/-}$). After it was determined that they were phenotypically identical, $Dnmt3a^{+/+}$, $Dnmt3a^{flox/+}$, and $Dnmt3a^{flox/flox}$ mice were grouped together and used as controls in data acquisition and statistical analysis. In $Dnmt3a_{Ctsk}^{-/-}$ and $Dnmt3a_{Rank}^{-/-}$ mice, as compared to control littermate mice, bone volume was greatly enhanced (**Fig. 1d**,**e**), and bone morphometric analysis revealed that osteoclast numbers as well as indicators of

osteoclastic bone resorption were lower, whereas the parameters for bone formation were normal (**Fig. 1f–i**). These results collectively suggest that osteoclast-specific *Dnmt3a* deficiency caused high bone mass due to a defect in osteoclast differentiation. In contrast, we observed no obvious abnormal bone phenotype in $Dnmt3a_{Col1a1}^{-/-}$ mice and no difference in osteoblast differentiation between $Dnmt3a_{Col1a1}^{-/-}$ mice and controls (**Supplementary Fig. 4**), suggesting that Dnmt3a expressed in osteoblasts does not affect bone phenotype.

RANKL-induced formation of TRAP-positive MNCs in $Dnmt3a_{Rank}^{-/-}$ BMMs was lower than in control BMMs (**Fig. 2a**), and the protein and mRNA expression of *Dnmt3a* were diminished in $Dnmt3a_{Rank}^{-/-}$ BMMs compared to control BMMs after RANKL treatment (**Fig. 2b**). Consistent with this, the expression of osteoclast-specific genes was also lower in $Dnmt3a_{Rank}^{-/-}$ BMMs compared to control BMMs after RANKL treatment (**Supplementary Fig. 5a**). Nevertheless, neither the number of $CD11b^{+}$ osteoclast precursor cells nor the proliferative and apoptotic activities of BMMs were affected by Dnmt3a deficiency (**Supplementary Fig. 5b**,**c**), indicating that $Dnmt3a_{Rank}^{-/-}$ BMMs contained a comparable number of osteoclast precursor cells to control BMMs. In $Dnmt3a_{Rank}^{-/-}$ BMMs, RANKL-induced actin ring and resorption pit formation were inhibited (**Supplementary Fig. 5d**,**e**). Taken together, these results suggest that Dnmt3a is required for osteoclast differentiation and bone resorption in a cell-autonomous manner. Although gene deletion occurred later in $Dnmt3a_{Ctsk}^{-/-}$ BMMs than in $Dnmt3a_{Rank}^{-/-}$ BMMs, results from an analysis of $Dnmt3a_{Ctsk}^{-/-}$ BMMs were otherwise similar to those from $Dnmt3a_{Rank}^{-/-}$ BMMs (**Supplementary Fig. 5f–i**). Thus, Dnmt3a is likely to function as a regulator in the middle stage of osteoclast differentiation.

To examine the importance of DNA methylation by Dnmt3a in osteoclast differentiation, we used a retroviral vector expressing Dnmt3a harboring mutations in the methyltransferase domain ($Dnmt3a^{P705V/C706D}$; ref. 21). Impaired osteoclast formation in $Dnmt3a_{Rank}^{-/-}$ BMMs after RANKL treatment was restored by the overexpression of WT Dnmt3a, but not catalytically inactive $Dnmt3a^{P705V/C706D}$ (**Fig. 2c**). These results suggest that DNA methylation by Dnmt3a is required for osteoclast differentiation.

Using models of bone resorptive disorders[22,23], we explored the possibility that modulation of Dnmt3a activity might be beneficial for controlling osteoporosis. First, to investigate the role of Dnmt3a in the pathological activation of osteoclastogenesis, we performed ovariectomy (OVX) (as a model of postmenopausal osteoporosis[24,25]) in 19-week-old $Dnmt3a_{Rank}^{-/-}$ female mice. The bone mass in $Dnmt3a_{Rank}^{-/-}$ OVX mice was higher than that in control OVX mice (**Fig. 2d**). Furthermore, the increase in osteoclast number induced by OVX was much lower in $Dnmt3a_{Rank}^{-/-}$ mice than in controls (**Fig. 2e**,**f**), suggesting a key role of Dnmt3a in the pathological activation of osteoclastogenesis. Next, to determine whether a Dnmt3a inhibitor has therapeutic efficacy in a model of osteoporosis, we examined the effect of TF-3 on bone loss in OVX mice. Injection of TF-3 into control mice 6 weeks after OVX protected against bone loss, which was associated with a lower number of osteoclasts as compared to the numbers in vehicle-injected (saline) OVX mice, but TF-3 had a negligible effect on bone mass and osteoclast number in $Dnmt3a_{Rank}^{-/-}$ OVX mice compared to vehicle-injected $Dnmt3a_{Rank}^{-/-}$ OVX mice (**Fig. 2d–f**), indicating that, in osteoclasts, TF-3 exerts its effect specifically on Dnmt3a. Taken together, these results suggest that inhibition of Dnmt3a-mediated epigenetic regulation is a potentially effective strategy for preventing bone loss.

Knowing that Dnmt3a functions as a transcriptional repressor in other cell types[21,26] we assessed the target(s) of Dnmt3a-mediated repression in osteoclastogenesis. To identify putative Dnmt3a-regulated genes, we performed genome-wide screening of mRNA expression and methylated DNA regions in control and $Dnmt3a_{Rank}^{-/-}$ BMMs after RANKL treatment. We initially selected genes that were downregulated during osteoclast differentiation in control cells. From those, we further selected genes in which the reduced expression was clearly normalized by *Dnmt3a* deficiency. In addition, we searched gene loci for sites whose methylation was increased more in control cells than in $Dnmt3a_{Rank}^{-/-}$ BMMs after RANKL treatment (**Supplementary Fig. 6a–c**). Several genes that are hypermethylated in osteoclasts have been identified[27], but no difference in the methylation of these genes occurred between control and $Dnmt3a_{Rank}^{-/-}$ BMMs after RANKL treatment (**Supplementary Fig. 6d**).

Our screening revealed 19 genes that met all criteria (**Supplementary Table 1**), and 8 of these genes were validated as genes whose expression is effected by RANKL stimulation by quantitative RT-PCR and methylated DNA immunoprecipitation (MeDIP)-qPCR analysis (**Fig. 3a** and **Supplementary Fig. 7a–c**). Gene expression–profiling analysis revealed that the expression of these genes was comparably lower in control and $Dnmt3a_{Rank}^{-/-}$ BMMs from 6 to 12 h after RANKL stimulation, whereas higher expression in $Dnmt3a_{Rank}^{-/-}$ BMMs was observed at 32 h (**Supplementary Fig. 7b**). These results suggest that Dnmt3a contributes to the maintenance of a stable repressive state during the middle stage of osteoclast differentiation rather than to the initiation of transcriptional silencing of these genes in osteoclast precursors. Of these genes, *Irf8*, *Gpr65* and *C1qc* are genes involved in osteoclast differentiation or function. Since Gpr65 and C1qc have only minor effects on osteoclast differentiation under physiological conditions[28,29], we focused on *Irf8* as its gene product is a known negative regulator of osteoclast differentiation[30].

The expression of *Irf8* in $Dnmt3a_{Ctsk}^{-/-}$ BMMs as well as $Dnmt3a_{Rank}^{-/-}$ BMMs was higher than in the corresponding control cells (**Fig. 3b** and **Supplementary Fig. 8a**,**b**). MBD-seq or a locus-specific methylation analysis by MeDIP-qPCR or bisulfate sequencing showed that two regions (hereafter referred to as DMR1 and DMR2) in the 3′-flanking region of the *Irf8* gene were hypomethylated in both $Dnmt3a_{Ctsk}^{-/-}$ and $Dnmt3a_{Rank}^{-/-}$ BMMs compared to the corresponding control cells (**Fig. 3c**,**d** and **Supplementary Fig. 8c–f**). Furthermore, chromatin immunoprecipitation (ChIP) analysis showed that Dnmt3a, but not Dnmt1 and Dnmt3b, bound to these regions after RANKL stimulation (**Supplementary Fig. 9a**). We found that RANKL induced *Irf8* downregulation, but the underlying epigenetic mechanism for this remains to be resolved. To test whether methylation of the DMRs affects *Irf8* promoter activity, we generated reporter constructs containing a DMR fragment with either unmethylated or methylated CpG sites. Reporter gene expression driven by the *Irf8* promoter was significantly suppressed in a methylated DMR-dependent manner (**Supplementary Fig. 9b**). Although both DMRs are likely to function as transcriptional silencers, they are located far from the *Irf8* gene body. A chromosome conformation capture (3C) assay, however, showed long-range interactions between DMRs and the 5′-flanking region of the *Irf8* gene after RANKL stimulation (**Supplementary Fig. 9c–e**). Taken together, these results suggest that *Irf8* is a direct repressive target of Dnmt3a-mediated DNA methylation during osteoclastogenesis.

To further clarify the importance of the Dnmt3a-Irf8 axis in osteoclastogenesis, we crossed $Dnmt3a_{Rank}^{-/-}$ mice with $Irf8^{-/-}$ mice to generate $Dnmt3a_{Rank}^{-/-}$ and $Irf8^{-/-}$ double knockout mice ($Dnmt3a_{Rank}^{-/-}Irf8^{-/-}$).

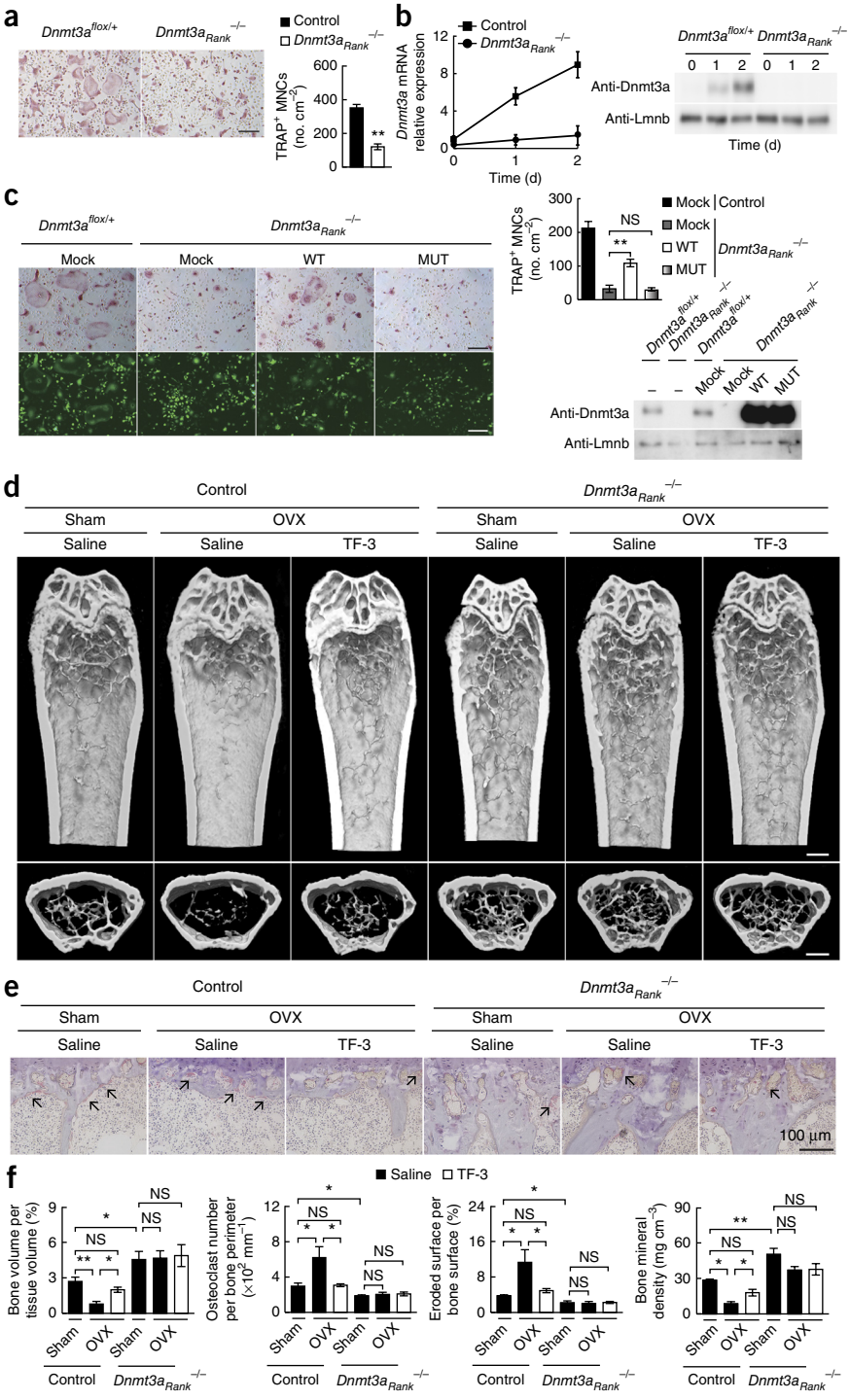

Figure 2 Deficiency of Dnmt3a impairs osteoclastogenesis and protects against pathological bone loss. (**a**) TRAP-stained cells showing osteoclast differentiation in control and *Dnmt3a*$_{Rank}^{-/-}$ BMMs. Scale bars, 100 μm (**a**,**c**,**e**). (**b**) Protein (immunoblot, right) and mRNA (graph, left) expression of Dnmt3a in control and *Dnmt3a*$_{Rank}^{-/-}$ BMMs stimulated with RANKL. Results representative of more than three experiments; expression relative to day 0. (**c**) Effect of retroviral Dnmt3a (WT) expression and catalytically inactive Dnmt3a$^{P705V/C706D}$ (mutant, MUT) on osteoclastogenesis of *Dnmt3a*$_{Rank}^{-/-}$ and control BMMs stimulated with RANKL. TRAP-stained cells (upper panels), bicistronic retrovirus vector–derived EGFP expression (lower panels), the number of TRAP-positive cells with more than three nuclei (graph, right) and protein expression of Dnmt3a in mock-infected or Dnmt3a variants–transduced cells (immunoblot, right) are shown. Mock, cells infected with a retrovirus containing control (pMX-IRES-EGFP). (**d**) The therapeutic effect of the Dnmt3a inhibitor TF-3 on ovariectomy (OVX)-induced bone loss. μCT of the femurs of 28-week-old sham-operated, saline-treated (sham), saline-treated OVX (saline) and TF-3–treated OVX (TF-3) control and *Dnmt3a*$_{Rank}^{-/-}$ mice are shown. $n > 4$ for each condition; scale bars, 0.5 mm. (**e**) Histological analysis of the proximal tibias of 28-week-old sham, saline-, and TF-3–treated OVX control and *Dnmt3a*$_{Rank}^{-/-}$ mice (TRAP-stained; red with arrows, osteoclasts). (**f**) Bone morphometric analysis of 28-week-old sham ($n = 5$), saline-treated OVX ($n = 4$), and TF-3–treated OVX control mice ($n = 5$); and sham ($n = 4$), saline-treated OVX ($n = 4$), and TF-3–treated OVX *Dnmt3a*$_{Rank}^{-/-}$ mice ($n = 4$) as well as bone mineral density by μCT analysis of 28-week-old sham ($n = 4$), saline-treated OVX ($n = 4$), and TF-3–treated OVX control mice ($n = 4$); and sham ($n = 5$), saline-treated OVX ($n = 5$), and TF-3–treated OVX *Dnmt3a*$_{Rank}^{-/-}$ mice ($n = 5$) (all females). Data denote the mean ± sem. $^{*}P < 0.05$; $^{**}P < 0.01$; NS, not significant (*t*-test in **a**, ANOVA in **c**,**f**).

Dnmt3a$_{Rank}^{-/-}$*Irf8*$^{-/-}$ mice had low bone mass due to a large number of osteoclasts compared with *Dnmt3a*$_{Rank}^{-/-}$ mice (**Fig. 3e**,**f**), indicating that *Irf8* may act downstream of *Dnmt3a* in the control of bone mass. In addition, *in vitro* osteoclastogenesis in *Dnmt3a*$_{Rank}^{-/-}$*Irf8*$^{-/-}$ cells was accelerated compared with that in *Dnmt3a*$_{Rank}^{-/-}$ cells (**Fig. 3g**). These results suggest that Dnmt3a exerts its inhibitory function by downregulating *Irf8*. Consistent with this idea, we found that treatment with TF-3 led to impaired *Irf8* downregulation with a concomitant decrease in DNA methylation at the *Irf8* gene locus (**Supplementary Fig. 10a**,**b**). Furthermore, *in vitro* osteoclastogenesis in TF-3–treated BMMs was accelerated by shRNA-mediated knockdown of *Irf8* (**Supplementary Fig. 10c**).

These observations strongly suggest that the RANKL-inducible expression of Dnmt3a is necessary to suppress *Irf8* via DNA methylation. To investigate the role of Dnmt3a, we tested the necessity of Dnmt3a for *Irf8* regulation. Overexpression of Dnmt3a did not affect the expression of *Irf8* or DNA methylation at the *Irf8* gene locus in non–RANKL-treated BMMs (**Fig. 4a**,**b**), indicating that Dnmt3a is not sufficient to completely regulate *Irf8* expression. Because Dnmt3a uses SAM as the methyl donor in the methylation reaction[1] (**Fig. 4c**), we measured SAM in osteoclast precursors and osteoclasts using capillary electrophoresis mass spectrometry (CE-MS). Notably, the level of SAM was significantly higher in BMMs stimulated with RANKL as compared to RANKL-unstimulated BMMs. (**Fig. 4d**). In contrast, the level of acetyl-CoA, which is the acetyl donor for acetyltransferase reactions (another epigenetic modifier), was not changed by RANKL stimulation. These results prompted us to examine the effect of

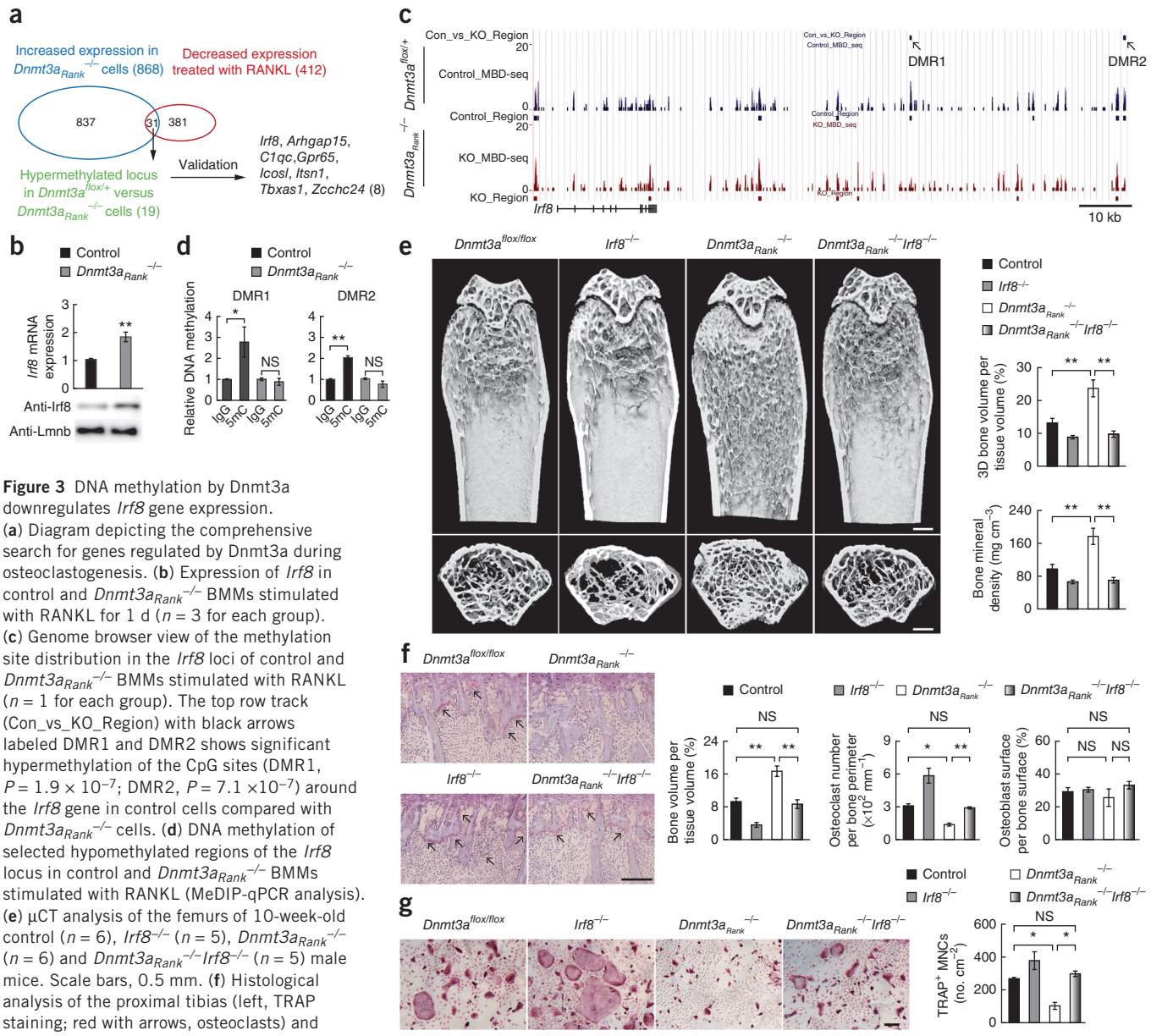

Figure 3 DNA methylation by Dnmt3a downregulates *Irf8* gene expression. (**a**) Diagram depicting the comprehensive search for genes regulated by Dnmt3a during osteoclastogenesis. (**b**) Expression of *Irf8* in control and $Dnmt3a_{Rank}^{-/-}$ BMMs stimulated with RANKL for 1 d ($n = 3$ for each group). (**c**) Genome browser view of the methylation site distribution in the *Irf8* loci of control and $Dnmt3a_{Rank}^{-/-}$ BMMs stimulated with RANKL ($n = 1$ for each group). The top row track (Con_vs_KO_Region) with black arrows labeled DMR1 and DMR2 shows significant hypermethylation of the CpG sites (DMR1, $P = 1.9 \times 10^{-7}$; DMR2, $P = 7.1 \times 10^{-7}$) around the *Irf8* gene in control cells compared with $Dnmt3a_{Rank}^{-/-}$ cells. (**d**) DNA methylation of selected hypomethylated regions of the *Irf8* locus in control and $Dnmt3a_{Rank}^{-/-}$ BMMs stimulated with RANKL (MeDIP-qPCR analysis). (**e**) μCT analysis of the femurs of 10-week-old control ($n = 6$), $Irf8^{-/-}$ ($n = 5$), $Dnmt3a_{Rank}^{-/-}$ ($n = 6$) and $Dnmt3a_{Rank}^{-/-}Irf8^{-/-}$ ($n = 5$) male mice. Scale bars, 0.5 mm. (**f**) Histological analysis of the proximal tibias (left, TRAP staining; red with arrows, osteoclasts) and parameters (right) for osteoclastic bone resorption and osteoblastic bone formation during bone morphometric analysis of 10-week-old control ($n = 5$), $Irf8^{-/-}$ ($n = 5$), $Dnmt3a_{Rank}^{-/-}$ ($n = 5$), and $Dnmt3a_{Rank}^{-/-}Irf8^{-/-}$ ($n = 5$) male mice. Scale bars, 100 μm (**f**,**g**). (**g**) Osteoclast differentiation from TRAP-stained control, $Irf8^{-/-}$, $Dnmt3a_{Rank}^{-/-}$ and $Dnmt3a_{Rank}^{-/-}Irf8^{-/-}$ BMMs. Data denote the mean ± sem. $^*P < 0.05$; $^{**}P < 0.01$; NS, not significant (*t*-test in **b**, ANOVA in **d**,**e**–**g**).

exogenous SAM on *Irf8* regulation. Overexpression of Dnmt3a led to lower *Irf8* expression as well as to higher DNA methylation at the *Irf8* gene locus in non–RANKL-treated BMMs when SAM was exogenously added as compared to mock-infected BMMs (**Fig. 4a**,**b**). However, in the osteoblast lineage, overexpression of Dnmt3a plus SAM did not affect DNA methylation because of a lack of recruitment of Dnmt3a to the *Irf8* gene locus (**Supplementary Fig. 11a–c**), suggesting that Dnmt3a binds to DMR1 and DMR2 in a cell type–specific manner. Although the interaction between Dnmt3a and histone H3 is disrupted by the trimethylation of histone H3 at lysine 4 (H3K4me3)[31], demethylation of H3K4me3 occurred during osteoclast differentiation (**Supplementary Fig. 11d–f**). Furthermore, Suv39h1, a protein involved in heterochromatic gene silencing[32], bound to the *Irf8* locus in a Dnmt3a-dependent manner (**Supplementary Fig. 11g–j**). Accordingly, this osteoclast-specific chromatin state might facilitate both the recruitment of Dnmt3a to the *Irf8* gene and the DNA methylation–mediated suppression of *Irf8* expression. Taken together, these results suggest that co-induction of Dnmt3a and SAM triggered by RANKL plays an important role in *Irf8* regulation.

These findings raised questions about the mechanism by which RANKL induces SAM production. Methionine adenosyltransferase (Mat) produces SAM from methionine and ATP, and both osteoclast precursor cells and osteoclasts solely expressed *Mat2a*, whose protein expression did not increase after RANKL stimulation (**Supplementary Fig. 12a**). ATP levels were significantly elevated and methionine levels were not changed by RANKL stimulation (**Supplementary Fig. 12b**), so RANKL-induced increases in ATP level likely leads to increased SAM production.

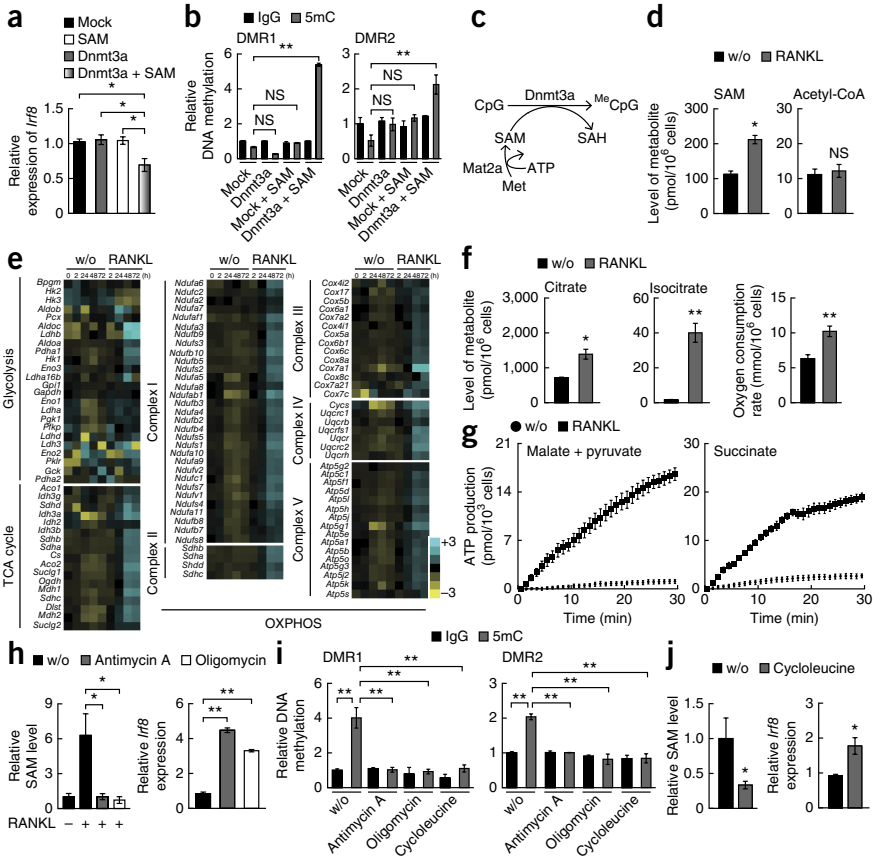

Figure 4 RANKL induces a metabolic shift toward oxidative metabolic processes in osteoclasts. (**a**) Effect of SAM on Dnmt3a-mediated *Irf8* suppression. (**b**) Effect of SAM (10 μM) on Dnmt3a-mediated DNA methylation of the *Irf8* gene locus (MeDIP-qPCR analysis). (**c**) The methionine metabolic pathway coupled to epigenetic regulation. (**d**) Levels of metabolites in BMMs stimulated with or without RANKL for 1 d. (**e**) Microarray data for expression of metabolic genes involved in glycolysis, the tricarboxylic acid (TCA) cycle and oxidative phosphorylation (OXPHOS) during osteoclastogenesis. (**f**) Levels of TCA-cycle metabolites (citrate and isocitrate) as well as the oxygen consumption rate in BMMs stimulated with or without RANKL for 1 d. (**g**) Malate plus pyruvate- and succinate-supported ATP synthesis in RANKL-treated or non-treated BMMs. (**h**) Effect of the respiratory chain inhibitors antimycin A (100 nM) and oligomycin (1 nM) on *Irf8* expression and SAM levels in BMMs stimulated with or without RANKL. (**i**) Effect of inhibitors on DNA methylation of the *Irf8* gene locus (MeDIP-qPCR analysis). (**j**) Effect of the Mat inhibitor cycloleucine (2 mM) on *Irf8* expression and SAM levels in BMMs stimulated with RANKL. Data denote the mean ± sem. $*P < 0.05$; $**P < 0.01$; NS, not significant (ANOVA in **a**,**b**,**h**,**i**, *t*-test in **d**,**f**,**j**).

ATP is manufactured in the mitochondria, and mitochondrial biogenesis is promoted during osteoclast differentiation[3]; however, the metabolic status of osteoclasts is not well characterized. To explore this process during osteoclast differentiation, we analyzed in RANKL-stimulated BMMs the expression pattern of metabolic enzymes involved in cellular respiration, which is divided into three metabolic processes: glycolysis, the tricarboxylic acid (TCA) cycle, and oxidative phosphorylation (OXPHOS). Most of the TCA- and OXPHOS-related genes exhibited a shared expression pattern characterized by a steady RANKL-dependent increase (**Fig. 4e** and **Supplementary Fig. 12c**). To determine whether these changes in gene expression could affect cellular metabolic activities in osteoclasts, we assayed metabolites in osteoclast precursors and osteoclasts using CE-MS. The levels of TCA cycle metabolites were significantly higher in BMMs stimulated with RANKL as compared to RANKL-unstimulated BMMs (**Fig. 4f** and **Supplementary Fig. 12d**,**e**). To determine the effect of RANKL on OXPHOS, we performed a mitochondrial ATP synthesis reconstitution assay with both permeabilized osteoclast precursors and osteoclasts whose mitochondria produced ATP via OXPHOS by supplementing ADP and substrates for respiratory chain reactions, such as succinate or malate plus pyruvate[33] (**Supplementary Fig. 12f**,**g**). Mitochondrial ATP synthesis activity was enhanced in BMMs stimulated with RANKL (**Fig. 4g** and **Supplementary Fig. 12h**). Consistent with this finding, the oxygen consumption rate was elevated in BMMs stimulated with RANKL as compared to RANKL-unstimulated BMMs (**Fig. 4f**). Taken together, these data suggest that the metabolic shift toward an oxidative process was accompanied by osteoclast differentiation. Because the gene expression profiles of metabolic enzymes, as well as mitochondrial ATP synthesis activity, were not enhanced during osteoblast differentiation (**Supplementary Fig. 13a–c**), this result is indicative of osteoclast-specific characteristics causing a metabolic shift toward oxidative metabolic processes.

Next we investigated whether RANKL-induced mitochondrial ATP production mediated *Irf8* gene expression via SAM upregulation. Treatment with the respiratory chain inhibitors antimycin A and oligomycin inhibited the mitochondrial ATP synthesis activity of osteoclasts (**Supplementary Fig. 12h**), and the level of ATP in RANKL-treated BMMs was also diminished by treatment with these inhibitors (**Supplementary Fig. 14a**). Treatment with each inhibitor prevented the upregulation of SAM and DNA methylation at the *Irf8* gene locus as well as the downregulation of *Irf8* expression (**Fig. 4h**,**i**). However, because ATP is an essential biomolecule for various cellular processes (such as signal transduction pathways including kinases), we could not exclude the possibility that other abnormalities linked to the inhibition of ATP affected SAM production. Indeed, although treatment with each inhibitor led to impaired TRAP-positive MNC formation, the inhibitory effect was not attenuated when SAM was exogenously added (**Supplementary Fig. 14b**). We also examined the Mat inhibitor cycloleucine, which abolished RANKL-induced *Irf8* downregulation and was associated with both lower SAM levels and a lower degree of DNA methylation at the *Irf8* gene locus as compared to BMMs not stimulated with cycloleucine (**Fig. 4i**,**j**). Furthermore, although treatment with this inhibitor led to impaired formation of TRAP-positive MNCs, the inhibitory effect was attenuated by exogenous SAM (**Supplementary Fig. 14b**). Taken together, these results suggest that the induction of SAM, which is coupled to RANKL-induced metabolic changes, plays an important role in *Irf8* regulation (**Supplementary Fig. 15**).

Our results show that DNA methylation, which was originally targeted for cancer therapies that inhibit tumor growth[34], is also emerging as a promising therapeutic target for treating bone resorptive disorders such as osteoporosis. Further, since the vicious cycle of bone

metastasis is a multistep process in which tumor cells and osteoclasts are intricately involved, targeted DNA methylation may also have dual benefits for the treatment of bone metastasis. Thus, therapeutic targeting of epigenetic regulation could open up a new avenue for the prevention and treatment of various bone disorders.

METHODS

Methods and any associated references are available in the online version of the paper.

Accession codes. GEO: GSE59387, GSE59388.

Note: Any Supplementary Information and Source Data files are available in the online version of the paper.

ACKNOWLEDGMENTS

We thank K. Kaseda, M. Shirazaki, and Y. Maijima for technical assistance and J. Kikuta, S. Fujimori, and S. Simmons for helpful discussions. We also thank M. Okano, S. Takeda, and G. Karsenty; H. Wu, M. Takami, and K. Ozato for the gifts of *Dnmt3a*-deficient ESCs, *Col1a1–Cre* transgenic mice, the Dnmt3a expression vector, and *Irf8*$^{-/-}$ mice, respectively. This work was supported by Grants-in-Aid for Scientific Research on Innovative Areas from the Japan Society for the Promotion of Science (JSPS) (26116719; K.N.); Grants-in-Aid for Creative Scientific Research and Young Scientists (A) from the JSPS (26713010; K.N.); Grants-in-Aid for Scientific Research (A) from the JSPS (25253070; M.I.); the Funding Program for World-Leading Innovative R&D on Science and Technology (FIRST Program) from the Ministry of Education, Culture, Sports, Science and Technology, Japan (MEXT; M.I.); the Platform for Drug Discovery, Informatics, and Structural Life Science from the MEXT, Japan (T.T., S. Kawaguchi and M.Y.); and grants from the Astellas Foundation for Research on Metabolic Disorders (K.N.), the Ichiro Kanehara Foundation (K.N.), the Shimadzu Science Foundation (K.N.), the Takeda Science Foundation (K.N. and M.I.), and the International Human Frontier Science Program (RGY0077/2011 to M.I.).

AUTHOR CONTRIBUTIONS

K.N. directed the project, conducted most of the experiments, and prepared the manuscript. Y.I. contributed to *in vitro* analyses. Y.K. supported the generation of osteoclast-specific *Dnmt3a* knockout mice. F.K. and M.Y. contributed to MBD-seq analyses. S. Kawaguchi and T.T. contributed to *in silico* analyses. T.N. and S. Kato generated *Ctsk*$^{Cre/+}$ mice. H.T. supported the GeneChip analysis. M.I. helped to direct the project and prepare the manuscript.

COMPETING FINANCIAL INTERESTS

The authors declare no competing financial interests.

1. Teperino, R., Schoonjans, K. & Auwerx, J. Histone methyl transferases and demethylases; can they link metabolism and transcription? *Cell Metab.* **12**, 321–327 (2010).
2. Lu, C. & Thompson, C.B. Metabolic regulation of epigenetics. *Cell Metab.* **16**, 9–17 (2012).
3. Ishii, K.A. *et al.* Coordination of PGC-1beta and iron uptake in mitochondrial biogenesis and osteoclast activation. *Nat. Med.* **15**, 259–266 (2009).
4. Theill, L.E., Boyle, W.J. & Penninger, J.M. RANK-L and RANK: T cells, bone loss, and mammalian evolution. *Annu. Rev. Immunol.* **20**, 795–823 (2002).
5. Xing, L., Schwarz, E.M. & Boyce, B.F. Osteoclast precursors, RANKL/RANK, and immunology. *Immunol. Rev.* **208**, 19–29 (2005).
6. Lorenzo, J., Horowitz, M. & Choi, Y. Osteoimmunology: interactions of the bone and immune system. *Endocr. Rev.* **29**, 403–440 (2008).
7. Jones, D., Glimcher, L.H. & Aliprantis, A.O. Osteoimmunology at the nexus of arthritis, osteoporosis, cancer, and infection. *J. Clin. Invest.* **121**, 2534–2542 (2011).
8. Karsenty, G. & Wagner, E.F. Reaching a genetic and molecular understanding of skeletal development. *Dev. Cell* **2**, 389–406 (2002).
9. Yasui, T., Hirose, J., Aburatani, H. & Tanaka, S. Epigenetic regulation of osteoclast differentiation. *Ann. NY Acad. Sci.* **1240**, 7–13 (2011).
10. Ross, F.P. & Teitelbaum, S.L. $\alpha_v\beta_3$ and macrophage colony-stimulating factor: partners in osteoclast biology. *Immunol. Rev.* **208**, 88–105 (2005).
11. Hayashi, M. *et al.* Osteoprotection by semaphorin 3A. *Nature* **485**, 69–74 (2012).
12. Nishikawa, K. *et al.* Blimp1-mediated repression of negative regulators is required for osteoclast differentiation. *Proc. Natl. Acad. Sci. USA* **107**, 3117–3122 (2010).
13. Mund, C., Brueckner, B. & Lyko, F. Reactivation of epigenetically silenced genes by DNA methyltransferase inhibitors: basic concepts and clinical applications. *Epigenetics* **1**, 7–13 (2006).
14. Rajavelu, A., Tulyasheva, Z., Jaiswal, R., Jeltsch, A. & Kuhnert, N. The inhibition of the mammalian DNA methyltransferase 3a (Dnmt3a) by dietary black tea and coffee polyphenols. *BMC Biochem.* **12**, 16 (2011).
15. Okano, M., Bell, D.W., Haber, D.A. & Li, E. DNA methyltransferases Dnmt3a and Dnmt3b are essential for *de novo* methylation and mammalian development. *Cell* **99**, 247–257 (1999).
16. Nguyen, S., Meletis, K., Fu, D., Jhaveri, S. & Jaenisch, R. Ablation of *de novo* DNA methyltransferase Dnmt3a in the nervous system leads to neuromuscular defects and shortened lifespan. *Dev. Dyn.* **236**, 1663–1676 (2007).
17. Kaneda, M. *et al.* Essential role for *de novo* DNA methyltransferase Dnmt3a in paternal and maternal imprinting. *Nature* **429**, 900–903 (2004).
18. Nakamura, T. *et al.* Estrogen prevents bone loss via estrogen receptor α and induction of Fas ligand in osteoclasts. *Cell* **130**, 811–823 (2007).
19. Maeda, K. *et al.* Wnt5a–Ror2 signaling between osteoblast-lineage cells and osteoclast precursors enhances osteoclastogenesis. *Nat. Med.* **18**, 405–412 (2012).
20. Dacquin, R., Starbuck, M., Schinke, T. & Karsenty, G. Mouse α1(I)-collagen promoter is the best known promoter to drive efficient Cre recombinase expression in osteoblast. *Dev. Dyn.* **224**, 245–251 (2002).
21. Wu, H. *et al.* Dnmt3a-dependent nonpromoter DNA methylation facilitates transcription of neurogenic genes. *Science* **329**, 444–448 (2010).
22. Rodan, G.A. & Martin, T.J. Therapeutic approaches to bone diseases. *Science* **289**, 1508–1514 (2000).
23. Goldring, S.R. & Gravallese, E.M. Bisphosphonates: environmental protection for the joint? *Arthritis Rheum.* **50**, 2044–2047 (2004).
24. Negishi-Koga, T. *et al.* Suppression of bone formation by osteoclastic expression of semaphorin 4D. *Nat. Med.* **17**, 1473–1480 (2011).
25. Shinohara, M. *et al.* Tyrosine kinases Btk and Tec regulate osteoclast differentiation by linking RANK and ITAM signals. *Cell* **132**, 794–806 (2008).
26. Li, E. Chromatin modification and epigenetic reprogramming in mammalian development. *Nat. Rev. Genet.* **3**, 662–673 (2002).
27. de la Rica, L. *et al.* PU.1 target genes undergo Tet2-coupled demethylation and DNMT3b-mediated methylation in monocyte-to-osteoclast differentiation. *Genome Biol.* **14**, R99 (2013).
28. Teo, B.H., Bobryshev, Y.V., Teh, B.K., Wong, S.H. & Lu, J. Complement C1q production by osteoclasts and its regulation of osteoclast development. *Biochem. J.* **447**, 229–237 (2012).
29. Hikiji, H. *et al.* TDAG8 activation inhibits osteoclastic bone resorption. *FASEB J.* **28**, 871–879 (2014).
30. Zhao, B. *et al.* Interferon regulatory factor-8 regulates bone metabolism by suppressing osteoclastogenesis. *Nat. Med.* **15**, 1066–1071 (2009).
31. Zhang, Y. *et al.* Chromatin methylation activity of Dnmt3a and Dnmt3a/3L is guided by interaction of the ADD domain with the histone H3 tail. *Nucleic Acids Res.* **38**, 4246–4253 (2010).
32. Paro, R. Chromatin regulation. Formatting genetic text. *Nature* **406**, 579–580 (2000).
33. Fujikawa, M. & Yoshida, M. A sensitive, simple assay of mitochondrial ATP synthesis of cultured mammalian cells suitable for high-throughput analysis. *Biochem. Biophys. Res. Commun.* **401**, 538–543 (2010).
34. Rodríguez-Paredes, M. & Esteller, M. Cancer epigenetics reaches mainstream oncology. *Nat. Med.* **17**, 330–339 (2011).

ONLINE METHODS

Mice and bone analysis. We generated and genotyped *Dnmt3a*$^{flox/flox}$, *Ctsk*$^{Cre/+}$, *RANK*$^{Cre/+}$, *Col1a1*–Cre and *Irf8*$^{-/-}$ mice as previously described[17–20,30]. *Dnmt3a*$^{+/+}$, *Dnmt3a*$^{flox/+}$ and *Dnmt3a*$^{flox/flox}$ littermate mice that did not carry the Cre recombinase were used as controls (and are referred to as such). There are no differences in bone phenotype among them. All mice were born and maintained under specific pathogen–free conditions, and all animal studies were approved by the Institutional Animal Care and Use Committee of Osaka University. All strains were on the C57BL/6 background. Ten-week-old sex-matched mice were used for experiments unless otherwise mentioned. Both male and female mice were used except when indicated (OVX experiments). Animals were randomly included in the experiments according to genotyping results. There were no animals excluded from the study. Animal experiments were conducted in a blinded fashion with respect to the investigator. The numbers of animals used per experiment are stated in the figure legends. Three-dimensional microcomputed tomography (μCT) analyses and bone morphometric analyses were performed as described previously[12].

Osteoporosis models of bone loss have been described previously[24]. 19-week-old female mice were ovariectomized or sham-operated. To analyze the therapeutic effect of TF-3, at 6 weeks after surgery, we started injection of TF-3 (8 mg kg^{-1} body weight). Mice were injected every 3 d for 3 weeks. All of the mice were killed and subjected to μCT and bone morphometric analyses 9 weeks after surgery.

Cell culture. *In vitro* osteoclast and osteoblast differentiation has been described previously[11,12]. Briefly, for *in vitro* differentiation, bone marrow–derived cells cultured with 10 ng/mL macrophage-colony stimulating factor (M-CSF) (R&D Systems and Miltenyi Biotec) for 2 d were used as osteoclast precursor cells and bone marrow–derived monocyte-macrophage precursor cells (BMMs), and were further cultured with 50 ng/mL RANKL (Peprotech) in the presence of 10 ng/mL M-CSF for 3 d. TRAP-positive multinucleated cells (MNCs; TRAP^{+} MNCs, more than three nuclei) were counted. We determined the rate of cell proliferation using the Cell Proliferation ELISA Kit (Roche) and detected apoptotic cells using the Cell Death Detection ELISA Kit (Roche). For the pit-formation assay, mature osteoclasts were formed after 4 d in culture. We collected osteoclasts on RepCell dishes (CellSeed) by incubation at 4 °C. Staining of resorption pits was performed as described previously[35]. All cells were removed by sonication and stained with 20 μg/mL WGA-lectin-peroxidase (Sigma-Aldrich) for 30 min. Bone slices were washed to remove unbound lectin, and DAB substrate was used to develop the stain.

For *in vitro* osteoblast differentiation, cells derived from bone marrow or calvaria were cultured with osteogenic medium (50 μM ascorbic acid, 10 nM dexamethasone, and 10 mM β-glycerophosphate). An ALP assay was performed after 7 d of culture and Alizarin Red staining was performed after 14 or 21 d of culture as described previously[11,36].

The generation of ESC-derived osteoclasts was described previously[37]. Briefly, ESCs were trypsinized and plated in hanging drops in an inverted Petri dish. Embryoid bodies were collected from hanging drops on day 2 and transferred to a tissue culture dish containing culture medium supplemented with 10 ng/mL M-CSF and 10 ng/mL IL-3. On day 11, the supernatant was removed and transferred to RepCell dishes containing culture medium supplemented with 10 ng/mL M-CSF for 3 d. Cells were detached by incubation at 4 °C and stimulated with 50 ng/mL RANKL and 10 g/mL M-CSF for 3 d.

Metabolite measurements. Extracts were prepared from ~2 × 10^{6} cells with methanol containing internal standard solution (Human Metabolome Technologies). Cationic compounds were measured in the positive mode of capillary electrophoresis–connected time-of-flight mass spectrometry (CE-TOFMS) and anionic compounds were measured in the positive and negative modes of CE-MS/MS. ATP and SAM in osteoclast precursors and osteoclasts were detected using the Kinshiro ATP Luminescence kit (CosmoBio) and Bridge-It SAM Fluorescence Assay Kit (Mediomics), respectively. Cell extracts were prepared by lysis in Kinshiro ATP extraction reagent (CosmoBio) to measure ATP in osteoclast precursors and osteoclasts, whereas cell extracts were prepared by 0.2% perchloric acid/0.08% 2-mercaptoethanol to measure SAM in osteoclast precursors and osteoclasts.

Flow cytometry analysis. Single-cell suspensions were incubated with anti-CD16/CD32 for 10 min, and then stained with Brilliant Violet–conjugated anti-CD11b (M1/70; eBioscience) in flow cytometry (FACS) buffer (1× phosphate-buffered saline (PBS), 4% heat-inactivated FCS, and 2 mM EDTA) for 15 min. Stained cells were analyzed on a FACSCanto II Flow Cytometer (BD Biosciences). FACS data were statistically analyzed with FlowJo software (TreeStar Inc.).

Quantitative RT-PCR analysis. Total RNA and cDNA were prepared using the RNeasy Mini Kit (Qiagen) and Superscript III reverse transcriptase (Invitrogen) according to the manufacturers' instructions. Real-time PCR was performed with a Thermal Cycler Dice Real Time System (TaKaRa Bio) using SYBR Premix EX Taq (TaKaRa Bio). The primer sequences are listed in **Supplementary Table 2**.

GeneChip analysis. GeneChip analysis was performed as described previously[11,12]. Briefly, total RNA was converted into cDNA by reverse transcription. Biotinylated cRNA was then synthesized by *in vitro* transcription. After cRNA fragmentation, hybridization with the mouse genome 430 2.0 array (Affymetrix) or the SurePrint G3 Mouse Gene Expression 8X60K microarray (Agilent) was performed. The core data set has been deposited in the Gene Expression Omnibus database with accession code GSE59387 or the Genome Network Platform (http://genomenetwork.nig.ac.jp/).

DNA methylation analysis. We prepared genomic DNA from cultured cells by overnight proteinase K treatment, phenol–chloroform extraction, ethanol precipitation, and RNase digestion. For bisulfate genomic sequencing, genomic DNA was subjected to bisulfate conversion with the EpiTect Bisulfate Kit (Qiagen). Following bisulfate PCR, the products were cloned into the pGEM-T Easy vector (Promega) and subjected to sequencing. The primer sequences are listed in **Supplementary Table 2**.

Before carrying out MBD-seq and methylated DNA immunoprecipitation (MeDIP)-quantitative PCR (qPCR) analysis, we sonicated genomic DNA to produce random fragments ranging in size from 300 to 1,000 bp. For MBD-seq analysis, methylated DNA was enriched from genomic DNA using the EpiXplore Methylated DNA Enrichment Kit (TaKaRa Bio), and sequencing was performed using the HiSeq2000 sequencing system (Illumina). All reads passing the quality controls were mapped onto the mm9 mouse genome assembly using Bowtie[38]. We used MACS[39] to identify genomic regions enriched with methylated DNA sequences. BedGraph files were generated and viewed using the UCSC Genome Browser. The MBD-seq data have been deposited in the Gene Expression Omnibus database (accession code GSE59388).

MeDIP-qPCR analysis was performed as described previously[40,41]. Briefly, we denatured the DNA and immunoprecipitated it with a monoclonal antibody against 5-methylcytidine (Abcam) in IP buffer (10 mM sodium phosphate, pH 7.0; 140 mM NaCl; 0.05% Triton X-100). We incubated the mixture with protein G magnetic beads (Thermo Scientific) and then washed it with IP buffer. We then recovered the methylated DNA by treatment with proteinase K followed by phenol–chloroform extraction and ethanol precipitation. We carried out real-time PCR reactions with input DNA and the immunoprecipitated methylated DNA using SYBR Premix EX Taq (TaKaRa Bio). To evaluate the relative enrichment of target sequences after MeDIP-qPCR, we calculated the ratios of the signals for immunoprecipitated DNA versus input DNA.

Chromatin immunoprecipitation (ChIP) assay. ChIP assays were performed with the ChIP Assay Kit (Upstate Biotechnology) according to the manufacturer's instructions with minor modifications described previously[12]. Briefly, BMMs stimulated with or without RANKL were fixed with paraformaldehyde. After quenching with glycine, cells were lysed and sonicated. Sonicated chromatin was incubated with anti-Dnmt1 (ab92453), anti-Dnmt3a (ab13888), anti-Dnmt3b (ab13604), anti-histone H3 (di- plus trimethyl K4; ab6000), anti-Hdac1 (ab7028), anti-Hdac3 (ab7030), anti-Suv39h1 (ab12405; Abcam unless indicated otherwise), anti-Mbd1 (SAB4800034; Sigma) or anti-PU.1 (CST#2266)(Cell Signaling Technology). We used normal mouse IgG or normal rabbit IgG (Santa Cruz Biotechnology) as a control. Immunoprecipitation was performed using protein G magnetic beads (Thermo Scientific).

doi:10.1038/nm.3774

After extensive washing, protein–DNA crosslinks were reversed, and the precipitated DNA was treated with proteinase K before phenol–chloroform extraction and ethanol precipitation. For ChIP analysis of exogenous FLAG-tagged Dnmt3a and FLAG-tagged Dnmt3a$^{\Delta ADD}$, sonicated chromatin was immunoprecipitated with anti-FLAG M2 affinity gel (Sigma-Aldrich). The primer sequences are listed in **Supplementary Table 2**.

Chromosome conformation capture (3C) assay. The 3C analysis was performed as described previously[42]. We fixed BMMs cultured with or without RANKL in 2% paraformaldehyde and then quenched the reaction with 0.125 M glycine. After centrifugation, we suspended the cells in lysis buffer (10 mM Tris–HCl, 10 mM NaCl, 0.2% Nonidet P-40, and 1× cOmplete Protease Inhibitor Cocktail (Roche)), pelleted the nuclei by centrifugation, resuspended them in buffer H (TaKaRa Bio) plus 0.3% sodium dodecyl sulfate (SDS), and incubated them at 37 °C. We added Triton X (1.8%) to sequester the SDS and incubated the nuclear samples at 37 °C. We added EcoRI (TaKaRa Bio) to digest the chromatin overnight at 37 °C. We carried out intramolecular ligation with 2.5 ng/μL chromatin in ligation buffer (TaKaRa Bio) plus 1% Triton X and T4 ligase (TaKaRa Bio) at 4 °C. We extracted DNA by isopropanol and ethanol precipitation after reversing cross-linking with proteinase K at 65 °C overnight. We carried out a nested PCR analysis. The primer sequences are listed in **Supplementary Table 2**.

Retroviral gene transfer. The retroviral vectors pMX-Dnmt3a-IRES-GFP, pMX-Dnmt3a$^{P705V/C706D}$-IRES-GFP, pMX-FLAG-Dnmt3a-IRES-GFP, and pMX-FLAG-Dnmt3a$^{\Delta ADD}$ -IRES-GFP were constructed by inserting DNA fragments encoding Dnmt3a, catalytically inactive Dnmt3a$^{P705V/C706D}$, FLAG-tagged Dnmt3a, and ADD domain–deleted FLAG-tagged Dnmt3a into pMX-IRES-GFP. The retroviral vectors pSIREN-shDnmt1, pSIREN-shDnmt3a, pSIREN-shDnmt3b, and pSIREN-shIrf8 were constructed by inserting annealed oligonucleotides into RNAi-Ready pSIREN-RetroQ (BD Biosciences). The oligonucleotide sequences are listed in **Supplementary Table 2**. pSIREN-shControl was constructed previously[12]. Retroviral packaging was performed by transfecting the plasmids into Plat-E cells using FuGENE6 as described previously[43]. Ten hours after inoculation with retroviruses, BMMs were stimulated with RANKL.

Immunoblot analysis. Cell lysates were subjected to immunoblot analysis using anti-Dnmt1 (ab92453; 1/2000 dilution), anti-Dnmt3a (ab13888; 1/2000 dilution), anti-Dnmt3b (ab13604; 1/2000 dilution), anti-IRF8 (ab93718; 1/2000 dilution), anti-Mat2a (ab77471; 1/2000 dilution) and anti-Lamin B (M-20; 1/2000 dilution) (all Santa Cruz Biotechnology). Nuclear proteins were prepared as previously described[44]. Whole-cell extracts were prepared by lysis in radioimmunoprecipitation assay (RIPA) buffer.

***In vitro* Dnmt and histone methyltransferase assays.** *In vitro* assays were performed with the DNMT1 Chemiluminescent Assay Kit, DNMT3A Chemiluminescent Assay Kit, DNMT3B Chemiluminescent Assay Kit, and Histone H3(K9) Universal Methyltransferase New Assay Kit (BPS Bioscience) according to the manufacturer's instructions. Procainamide and RG108 were purchased from Sigma-Aldrich and Abcam, respectively, whereas TF-3 and EGCG were purchased from Wako Chemical.

***In silico* docking simulation of DNMT3A and potent inhibitors.** To calculate the binding affinity between Dnmt3a and potent chemicals including RG108, ECGC, and TF3 with Molegro Virtual Docker 6.0.0, we obtained crystal structure data for DNMT3A from the RCSB Protein Data Bank (PDB ID: 2QRV). The binding motifs of these proteins were also predicted and drawn with Molegro Virtual Docker 6.0.0. To determine the binding affinity, we used the MolDock score from MolDock Optimizer using default settings. The number of trial runs for calculations was 20. The chemical structures of ligands including RG108, EGCG, and TF were drawn using ChemBioDraw Ultra 13.0 and optimized by MM2 calculations in Chem3D Pro 13.0. For the hDNMT3A docking search space, X = 108.64, Y = 44.13, Z = 1.50, and R = 18.

Mitochondrial ATP synthesis (Masc) assay. The Masc assay was performed as described previously[33]. Briefly, we collected osteoclast precursors and osteoclasts on RepCell dishes (CellSeed) by incubation at 4 °C. Then the cells were treated with a permeabilization buffer (0.18 mg/mL activated streptolysin O (SLO), 25 mM HEPES–KOH (pH 7.3), 125 mM potassium acetate, 2.5 mM magnesium acetate, 1 mM DTT, and a protease inhibitor cocktail (Roche)) and washed twice in a transportation buffer (25 mM HEPES–KOH buffer (pH 7.4), containing 115 mM potassium acetate, 2.5 mM $MgCl_2$, 1 mM DTT, 2 mM EGTA, and a protease inhibitor cocktail). The cells were incubated at 37 °C for 10 min and washed twice with buffer A (25 mM Tris–HCl (pH 7.4), 150 mM KCl, 2 mM EDTA, 0.1% bovine serum albumin, 10 mM potassium phosphate, and 0.1 mM $MgCl_2$). Buffer A containing 150 μM diadenosine pentaphosphate (Ap5A) was added to SLO-permeabilized cells, whereas buffer A containing 5 mM sodium succinate, 100 μM ADP, 5 mM MgCl2, 1× luciferin/luciferase mixture (Roche), and 1% dimethyl sulfoxide was added to start the assay. Succinate was replaced with a combination of 1 mM disodium malate and 1 mM sodium pyruvate.

Measurement of the oxygen consumption rate (OCR). Bone marrow–derived cells were seeded on RepCell dishes containing culture medium supplemented with M-CSF for 2 d and then were further cultured with RANKL in the presence of M-CSF for 1 d. Cells were detached by incubation at 4 °C and subjected to OCR analysis using the Fluorescence Lifetime Micro Oxygen Monitoring System (Instech).

Reporter gene assay. DMR fragments were isolated from genomic DNA and methylated using M.*SssI* CpG methyltransferase. The DNA fragments of unmethylated or methylated DMR regions were ligated to the 3′ end of *Irf8*-luc, which was constructed by subcloning a 1 kb fragment of the 5′ flanking region of the *Irf8* gene into the pGL4.20 (luc2/Puro) vector. The luciferase assay was performed in NIH3T3 cells transfected using Lipofectamine 2000 reagent (Invitrogen). After 30–36 h, dual luciferase activity was measured according to the manufacturer's protocols (Promega).

Statistical analysis. All data are expressed as mean ± sem. Statistical analysis was performed using the unpaired two-tailed Student's *t*-test for comparisons between two groups and analysis of variance (ANOVA) with the Bonferroni *post hoc* test for comparisons among three or more groups (throughout the paper, $*P < 0.05$; $**P < 0.01$; NS, not significant). All data met the assumption of statistical tests and had a normal distribution, and variance was similar between groups that were statistically compared. Replicates used were biological replicates, which were measured by using different samples derived from distinct mice. The results are representative examples of more than three independent experiments. We estimated the sample size considering the variation and mean of the samples. We tried to reach the conclusion using as small a size of samples as possible. We usually exclude samples if we observe any abnormality in terms of size, weight or apparent disease symptoms in mice before performing experiments. However, we did not exclude animals here, as we did not observe any abnormalities in the present study.

35. Selander, K., Lehenkari, P. & Vaananen, H.K. The effects of bisphosphonates on the resorption cycle of isolated osteoclasts. *Calcif. Tissue Int.* **55**, 368–375 (1994).
36. Nishikawa, K. *et al.* Maf promotes osteoblast differentiation in mice by mediating the age-related switch in mesenchymal cell differentiation. *J. Clin. Invest.* **120**, 3455–3465 (2010).
37. Nishikawa, K., Iwamoto, Y. & Ishii, M. Development of an *in vitro* culture method for stepwise differentiation of mouse embryonic stem cells and induced pluripotent stem cells into mature osteoclasts. *J. Bone Miner. Metab.* **32**, 331–336 (2014).
38. Langmead, B., Trapnell, C., Pop, M. & Salzberg, S.L. Ultrafast and memory-efficient alignment of short DNA sequences to the human genome. *Genome Biol.* **10**, R25 (2009).
39. Zhang, Y. *et al.* Model-based analysis of ChIP-Seq (MACS). *Genome Biol.* **9**, R137 (2008).
40. Weber, M. *et al.* Chromosome-wide and promoter-specific analyses identify sites of differential DNA methylation in normal and transformed human cells. *Nat. Genet.* **37**, 853–862 (2005).
41. Xu, Y. *et al.* Tet3 CXXC domain and dioxygenase activity cooperatively regulate key genes for Xenopus eye and neural development. *Cell* **151**, 1200–1213 (2012).
42. Murrell, A., Heeson, S. & Reik, W. Interaction between differentially methylated regions partitions the imprinted genes Igf2 and H19 into parent-specific chromatin loops. *Nat. Genet.* **36**, 889–893 (2004).
43. Morita, S., Kojima, T. & Kitamura, T. Plat-E: an efficient and stable system for transient packaging of retroviruses. *Gene Ther.* **7**, 1063–1066 (2000).
44. Nishikawa, K. *et al.* Self-association of Gata1 enhances transcriptional activity *in vivo* in zebra fish embryos. *Mol. Cell. Biol.* **23**, 8295–8305 (2003).